International Journal of Disaster Risk Science (2026) 17:128–147
https://doi.org/10.1007/s13753-025-00683-w

www.ijdrs.com
www.springer.com/13753

ARTICLE

Assessing and Optimizing Urban Dynamic Resilience to Extreme Rainfall from Shock to Recovery

Linmei Zhuang[1,2,3] · Ming Wang[1] · Kai Liu[1] · Loon Ching Tang[3] · Jidong Wu[1] · Dingde Xu[4] · Junfei Liu[1,2] · Jiawang Zhang[1] · Jiarui Yang[1] · Yi Ren[5] · Dong Xu[6]

Accepted: 13 November 2025 / Published online: 22 January 2026

Abstract

Climate change has intensified extreme rainfall events, challenging progress toward SDG 11's urban resilience targets. Current assessment methods often neglect dynamic recovery processes and regional precipitation disparities. We propose a three-phase framework combining interpretable machine learning (ML) and factorial experiments, using the Prep_shock index that integrates standardized rainfall intensity, capital exposure, and historical probability, to evaluate the dynamic resilience of 220+ Chinese cities from 2019 to 2022. Key findings reveal that: (1) The Prep_shock index effectively eliminates north-south precipitation biases, identifying Shandong coastal cities and Yangtze River Delta city clusters (36.2%) as high-resilience areas, in contrast to Henan Province. COVID-19 exacerbated systemic risks in megacities, undermining their capital protection capacities. (2) Spatial diagnostics classify 75.6% of the cities into Quadrant III (the balanced resilience category), with recovery times decreasing from the west to the east. Super-large cities like Zhengzhou (2021) exhibited critical recovery deficiencies (Quadrant IV). (3) Interpretable ML models (XGBoost/EBM) identify redundancy as the dominant resilience driver—robustness governs baseline resilience, while recovery relies on emergency support (for example, hospital beds density and fiscal inputs) and redundant infrastructure (for example, road network density). (4) Factorial experiments reveal optimization trade-offs: simultaneous enhancement of rapidity and redundancy diminishes their individual benefits, necessitating context-specific prioritization. The study advances dynamic resilience assessment methods and proposes quadrant-specific strategies for tailored urban adaptation.

Keywords Dynamic assessment · Extreme rainfall · Factorial analysis · Machine learning · Resilience optimization · Urban resilience

1 Introduction

Extreme rainfall events driven by climate change are reshaping urban disaster risk landscapes at an accelerating and unexpected pace. According to disaster statistics from the United Nations Office for Disaster Risk Reduction (UNDRR), the number of major global flood events surged from 1389 during 2000 to 3254 during 2019—an increase of 134% (UNDRR 2021). China, one of the countries most severely affected by flooding, faces mounting challenges to urban resilience due to the compounding effects of its monsoonal climate and rapid urbanization (Qian et al. 2024; Zhuang, Zhang, et al. 2024). Therefore, fulfilling the objectives of Sustainable Development Goal 11 (SDG 11) and the "Making Cities Resilient 2030" (MCR2030) initiative urgently requires scientifically grounded strategies for

✉ Ming Wang
wangming@bnu.edu.cn

1 School of National Safety and Emergency Management, Beijing Normal University, Beijing 100875, China

2 Faculty of Geographical Science, Beijing Normal University, Beijing 100875, China

3 Department of Industrial Systems Engineering and Management, National University of Singapore, Singapore 117576, Singapore

4 College of Management, Sichuan Agricultural University, Chengdu 611130, China

5 School of Economics and Management, Sichuan Normal University, Chengdu 610101, China

6 Department of Geography, National University of Singapore, Singapore 119077, Singapore

assessing and enhancing urban resilience to extreme rainfall (Hemmati et al. 2022).

Resilience theory offers a valuable interdisciplinary framework for addressing this challenge. Since Holling (1973) first introduced the concept of ecological resilience, the theory has evolved through three key stages. In the engineering resilience phase, research focused on the mechanical resistance thresholds of infrastructure systems (Holling 1996). Subsequently, the theory of complex adaptive systems (Gunderson and Holling 2002) introduced dynamic, non-equilibrium models of resilience, laying the foundation for understanding the nonlinear response mechanisms of urban systems. This theoretical shift enabled the emergence of social-ecological resilience (Folke 2006), which challenged the single-stability assumption by emphasizing the adaptive capacity of multiple actors. This conceptual evolution continues, with recent reviews highlighting that definitions of flood resilience are becoming increasingly diverse, expanding from merely "coping" to encompass critical components such as "recovery" and "adaptation" (Laidlaw and Percival 2024). Although recent studies have developed multidimensional indicator-based frameworks (Meerow et al. 2016), significant limitations remain in the context of extreme rainfall. First, most assessments rely on static, cross-sectional models (Moghadas et al. 2019), failing to capture the time-varying dynamics of post-disaster recovery. Second, institutional factors such as fiscal resource allocation are often excluded from the evaluation, a gap particularly evident in developing countries like China (Gilmore et al. 2022; Sadler et al. 2024).

In parallel with assessment challenges, current attribution methods also face limitations in capturing the complexity of urban systems. Mainstream machine learning models—such as SHAP-based XGBoost—are capable of handling high-dimensional and nonlinear data (Lundberg and Lee 2017), but their black-box nature often obscures decision-making mechanisms and makes it difficult to quantify multifactor interactions, such as the synergy between fiscal investment and drainage network density. Factorial experiments, as a classical approach in experimental design, enable precise identification of the direction and magnitude of interaction effects through systematic manipulation of variable levels (Box et al. 2005). However, this method suffers from the curse of dimensionality when applied to complex urban systems. This inherent trade-off between interpretability and complexity significantly constrains the precision and effectiveness of resilience policy interventions.

In response to these limitations, recent cutting-edge research has increasingly focused on leveraging dynamic modeling and artificial intelligence (AI) to better capture the complex, time-dependent nature of urban resilience (Khoshkonesh et al. 2024; Qin et al. 2025). For instance, studies have begun to integrate real-time sensor data and high-resolution satellite imagery with advanced machine learning algorithms to create more adaptive and predictive resilience assessment frameworks (Yabe et al. 2022; Li et al. 2025; Li, Zhou, et al. 2025). This new frontier emphasizes a shift from static vulnerability snapshots to a continuous understanding of system performance under stress, often employing digital twins and sophisticated simulation environments to model cascading failures and recovery pathways (Therias and Rafiee 2023; Zhuang, Wang, et al. 2024). While these advancements provide powerful predictive capabilities, a significant challenge remains in untangling the complex, nonlinear interactions between resilience drivers and in translating these "black-box" findings into actionable, interpretable policy, a gap which this study aimed to address (Cao 2023).

To address the aforementioned research gaps, this study integrates complex systems theory with interpretable artificial intelligence techniques, achieving methodological advances on three levels. First, we develop a dynamic assessment model of extreme rainfall exposure by integrating nationwide daily precipitation data (2019–2022) with gridded fixed capital stock. Second, drawing on the "4R" resilience framework (Bruneau et al. 2003), we construct a three-dimensional indicator system comprising robustness, rapidity, and redundancy, and establish a dynamic quantification system based on recovery functions. Finally, we propose a hybrid attribution analysis framework that combines interpretable machine learning with factorial experimental design to systematically identify both the independent and interaction effects of resilience determinants.

2 Material and Methods

This section details the comprehensive methodology employed to assess and analyze urban dynamic resilience. We first establish the theoretical and quantitative framework for resilience assessment, then describe the indicator system and data sources used for our empirical analysis. Finally, we outline the interpretable machine learning models and factorial experiment design used for the attribution analysis to identify the key drivers of resilience and their interactions.

2.1 The Framework of Resilience Assessment

This subsection outlines the conceptual and quantitative architecture for assessing dynamic resilience. It is structured into three core components: first, the adaptation of the "4R" theoretical framework to the context of urban flood resilience; second, the mathematical formulation of the post-disaster recovery process using a gamma function family; and third, the development of the multidimensional indicator system used to measure resilience attributes empirically.

2.1.1 Theoretical Framework

The theoretical foundation of this study is built upon the "4R" framework, which characterizes a system's overarching resilience capacity through a set of core attributes: Robustness, Rapidity, Redundancy, and Resourcefulness (Bruneau et al. 2003; Tierney and Bruneau 2007). These attributes are the essential properties exhibited by a resilient system's various dimensions (for example, social, economic, infrastructural, and governance) when confronted with a shock.

Robustness refers to the capacity of urban physical and social systems to withstand extreme events, such as the design standards of drainage infrastructure and the rainfall-resistance performance of buildings (Tierney and Bruneau 2007). Rapidity captures the speed at which essential functions recover post-disaster—for example, the time required to restore transportation networks and power supply—where delays can significantly amplify resilience losses (Rose 2007). Redundancy involves the presence of backup systems (for example, emergency pumping stations, multi-route transportation networks) that prevent cascading failures due to the malfunction of a single node (Ouyang and Dueñas-Osorio 2014). Resourcefulness reflects the system's capacity for resource mobilization and adaptive decision making, such as real-time flood response coordination enabled by timely data and cross-sectoral emergency mechanisms (Silverman et al. 2022). While these attributes provide a comprehensive qualitative description of resilience, a quantitative assessment requires a method to integrate their combined effect on system performance over time, which is often conceptualized using a recovery curve, as captured by the Resilience Triangle theory (Fig. 1). Within this "4R" framework, a clear distinction can be made between the different phases of a resilience event. The initial processes of resistance and absorption are analytically captured by the Robustness attribute, which governs the magnitude of performance loss immediately following a shock. The subsequent Recovery process is then shaped by the Rapidity and Redundancy attributes, which determine the speed and trajectory of the system's return to functionality.

To quantify resilience, this study integrates the recovery curve approach with the "4R" framework. Specifically, the area enclosed by the recovery curve of system performance ($P(t)$) and the pre-disaster baseline represents the magnitude of resilience loss (Bruneau et al. 2003) (Eq. 1), a method widely used to capture dynamic post-disaster recovery processes. The Resilience Triangle, by measuring the total performance loss over time, thus serves as an integrated metric that analytically combines the effects of initial resistance and absorption with the subsequent recovery. For instance, Klise (2023) applied recovery curves to assess the resilience of urban drinking water infrastructure under population growth and extreme weather disturbances. Zhang et al. (2024) constructed a global urban resilience model using nighttime light data, revealing that socioeconomic factors—such as income levels and governance capacity—significantly influence recovery speed, thus providing cross-regional empirical validation for the Resilience Triangle. Further applications of this theory in fields such as power systems (Hosseini et al. 2016), public health (Han et al. 2024), and public transportation (Wang et al. 2022) suggest that resilience loss reflects not only physical restoration efficiency, but also the interplay of social vulnerability (for example, unequal access to resources in low-income communities) and institutional shortcomings (for example, fragmented emergency planning) (Meerow and Newell 2019). Recent research trends emphasize integrating the "4R" framework with multi-source data—including meteorological and economic data—to uncover how complex urban systems adapt and recover under extreme rainfall events.

$$Resilience = \int_{t_0}^{t_1} [1 - P(t)]dt \tag{1}$$

2.1.2 Recovery Function

The concept of recovery is central to resilience, yet it is also considered one of the most challenging aspects to measure, with a notable lack of clarity on temporal scales in existing research (McClymont et al. 2020). To address this gap and precisely capture these time-varying dynamics, the recovery function employed in this study contains four key parameters—a, b, c, and d—each corresponding to one dimension of the "4R" resilience framework (Fig. 1). By constructing an indicator system and applying weighted calculations for each parameter, we derive the relative values of the 4R components for all Chinese cities. These relative scores are then mapped onto appropriate parameter ranges to shape city-specific recovery curves. Weights for each parameter were determined objectively using the CRITIC method. This technique was chosen for its ability to handle the interdependencies among resilience indicators by balancing both their variability and correlation (Diakoulaki et al. 1995). The detailed algorithmic procedure and justification for this choice are provided in Supplementary Material, Section 2.[1] Since we assume that cities are capable of recovering to their pre-disaster performance levels, the parameter d is fixed at 1 in all scenarios.

We adopt the gamma family as the functional form for modeling post-disaster urban recovery (Cassottana et al. 2019; Tang and Shen 2024). This function family satisfies the essential properties of asymptotic stability and

[1] https://doi.org/10.5281/zenodo.17798716

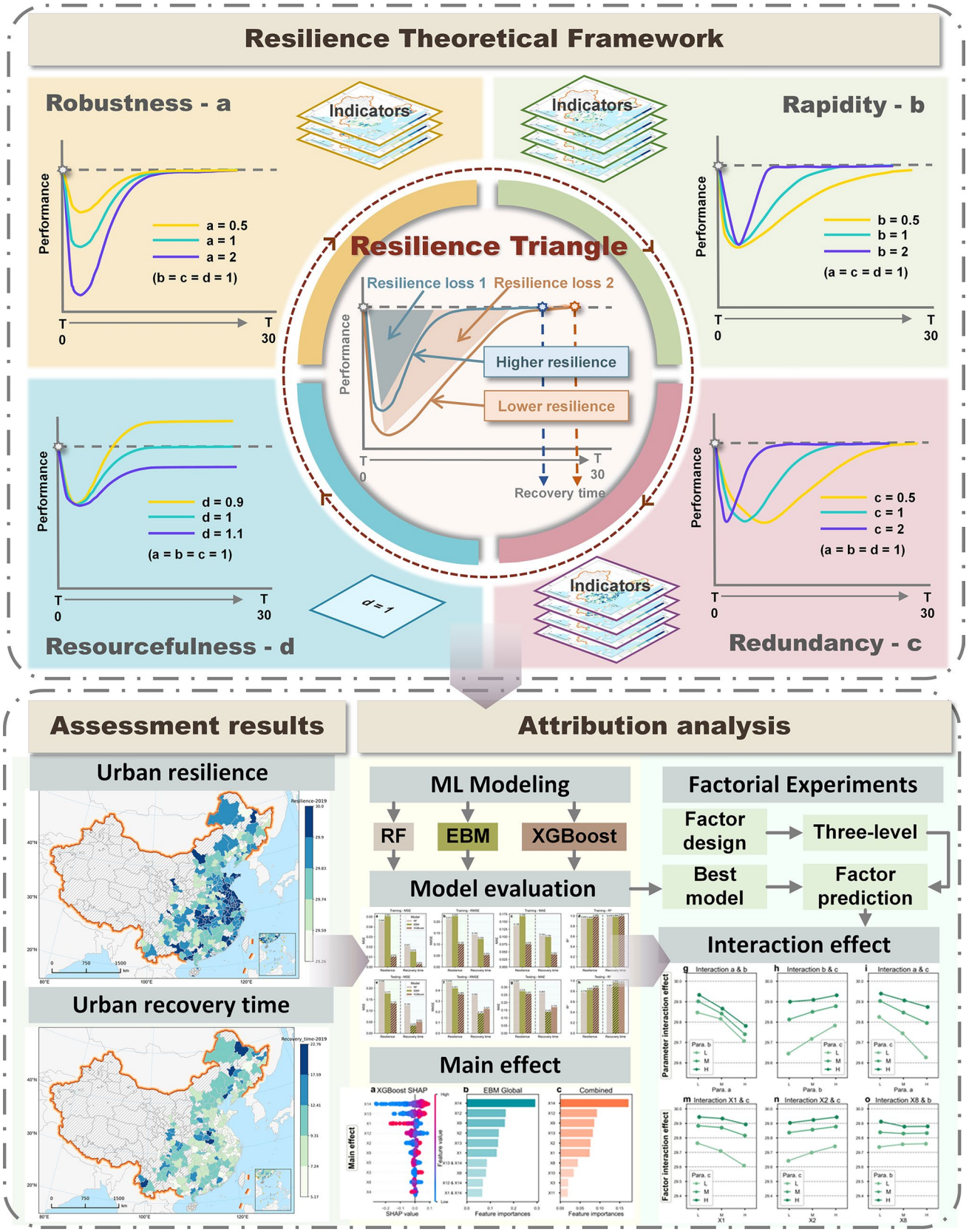
Resilience Theoretical Framework
Robustness - a
Indicators
Performance
a = 0.5
a = 1
a = 2
(b = c = d = 1)
T
0
T
30
Indicators
Rapidity - b
Performance
b = 0.5
b = 1
b = 2
(a = c = d = 1)
Resilience Triangle
Resilience loss 1
Resilience loss 2
Performance
Higher resilience
Lower resilience
Recovery time
Performance
d = 0.9
d = 1
d = 1.1
(a = b = c = 1)
d = 1
Resourcefulness - d
Indicators
Performance
c = 0.5
c = 1
c = 2
(a = b = d = 1)
Redundancy - c
Assessment results
Attribution analysis
Urban resilience
Urban recovery time
ML Modeling
RF
EBM
XGBoost
Model evaluation
Main effect
a XGBoost SHAP
b EBM Global
c Combined
SHAP value
Feature importances
Factorial Experiments
Factor design
Three-level
Best model
Factor prediction
Interaction effect
Parameter interaction effect
Factor interaction effect

◂**Fig. 1** A schematic diagram of research theory and framework. The parameter variations shown in the subplots are for illustrative purposes to demonstrate the mathematical function of each parameter. Within this functional form, parameters a and d are inverse indicators of their conceptual counterparts: a higher value of a corresponds to lower robustness (a larger initial drop), and a higher value of d corresponds to lower resourcefulness (a lower final recovery level). In our main analysis, d is fixed at 1 to model full recovery. *ML* Machine learning, *RF* Random forest, *EBM* Explainable boosting machine, *XGBoost* Extreme gradient boosting

quasi-convexity, making it suitable for capturing realistic recovery dynamics. The gamma family is constructed as an affine combination of two gamma functions (Eq. 2), where $P(t_0)$ denotes the pre-disaster performance level, and a, b, c, and d are the parameters to be estimated.

$$P(t) = P(t_0) - a\left\{\Gamma[d+1] - \Gamma\left[d + f(t|b,c)\right]\right\}, \quad a,b,c,d \geq 0 \tag{2}$$

Here, parameter a, which conceptually functions as an inverse measure of robustness, acts as a direct multiplier outside the gamma function terms, linearly scaling the overall magnitude (depth) of the performance loss curve $Loss(t) = a \cdot \left\{\Gamma[d+1] - \Gamma\left[d + f(t|b,c)\right]\right\}$. While the term within the braces dictates the temporal profile of the loss, parameter a controls its vertical scale. Consequently, a larger a corresponds mathematically to lower Robustness. $\Gamma(z)$ is the gamma function (Eq. 3), and $f(t|b,c)$ is a differentiable, non-increasing time-dependent function. Considering the urgency of post-disaster recovery, we specify $f(t)$ as an exponential function (Eq. 4), which satisfies $f(t=0|b,c) = 1$ and $\lim_{t\to\infty} f(t|b,c) = 0$. Figure 1 illustrates how the gamma family can simulate diverse recovery trajectories under different resilience scenarios.

$$\Gamma(z) = \int_0^\infty x^{z-1} \exp[-x]dx \tag{3}$$

$$f_{\text{Exp}}(t|b,c) = \exp[-ct^b] \tag{4}$$

To understand the role of parameter d, we analyze the function's limit as time approaches infinity ($t \to \infty$). Under this condition, the time-dependent decay function $f(t|b,c) = \exp[-ct^b]$ approaches 0. Therefore, the final steady-state performance level $P(\infty)$ can be expressed as Eq. 5.

$$P(\infty) = P(t_0) - a \cdot \{\Gamma[d+1] - \Gamma[d+0]\} = P(t_0) - a \cdot \{\Gamma[d+1] - \Gamma[d]\} \tag{5}$$

Utilizing the fundamental property of the gamma function, $\Gamma[z+1] - z\Gamma[z]$, we can simplify the performance loss term within the braces (Eq. 6).

$$\Gamma[d+1] - \Gamma[d] = d\Gamma[d] - \Gamma[d] = (d-1)\Gamma[d] \tag{6}$$

Substituting this back yields the final expression for the steady-state performance (Eqs. 7 and 8).

$$P(\infty) = P(t_0) - Loss(\infty) \tag{7}$$

$$Loss(\infty) = a \cdot (d-1)\Gamma[d] \tag{8}$$

In these equations for the final state, the term $Loss(\infty)$ represents the permanent performance loss at the end of the recovery process. It is crucial to note that this analysis, involving scenarios where $d \,!= 1$, is presented solely to theoretically demonstrate how parameter d mathematically governs the final recovery level and thus relates to resourcefulness. For the main analysis in this study, we consistently assume $d = 1$ for all cities. This ensures the permanent performance loss term $Loss(\infty)$ becomes exactly zero ($a \cdot (1-1)\Gamma[1] = 0$), thereby modeling full recovery $\left(P(\infty) = P(t_0)\right)$ and allowing for standardized cross-city comparison.

2.2 Indicator System

The development of our indicator system involved a systematic, multi-stage screening process to ensure theoretical rigor and contextual relevance. First, the process was anchored in the "4R" theoretical framework and built upon established indicator systems, including Berke and Campanella (2006), Chelleri et al. (2015), and the Disaster Resilience of Place (DROP) model (Cutter et al. 2008). Subsequently, each potential indicator was critically evaluated for its specific relevance to the challenges of extreme rainfall, ensuring a direct, literature-supported link to urban disaster resistance, emergency response efficiency, or recovery potential. The final selection was then confirmed based on the availability and measurability of consistent data across our large urban sample. This structured approach led to the development of an indicator system organized around three key dimensions: disaster resistance, emergency response efficiency, and substitution potential during disruption. The indicator design logic and its targeted relevance to rainfall impacts are elaborated across three resilience dimensions—robustness, rapidity, and redundancy—as summarized in Table 1. These indicators span multiple urban subsystems, including economic, social, static infrastructural, and dynamic environmental components (McClymont et al. 2020; Laidlaw and Percival 2024).

Table 1 Urban resilience assessment indicator system based on the "4R" framework

Resilience dimension	Function parameter	Factor name	Factor code	Description (attribute)	Unit	References
Robustness	*a* (X12) (an inverse measure of robustness)	Economic impact of extreme rainfall	X1	Cumulative capital exposure under relative daily extreme rainfall shocks at the grid scale (+)	%	Cao et al. (2023), Gu et al. (2025), and Kotz et al. (2022)
		Drainage network density	X2	Density of the drainage pipeline network in each city (–)	km/km^2	Li and Burian (2023), Wang et al. (2021), and Xu, Zhang, et al. (2024)
		Proportion of cumulative flood control investment	X3	Proportion of cumulative flood control investment in total municipal infrastructure investment (–)	%	Liao et al. (2019), and Liu et al. (2025), and Wu et al. (2024)
Rapidity	*b* (X13)	Total factor productivity	X4	Output efficiency and technological progress under given inputs (e.g., capital and labor) (+)	%	Tang et al. (2023) and Tang and Shen (2024)
		Proportion of fiscal expenditure on disaster prevention and emergency management	X5	Proportion of annual local fiscal expenditure allocated to disaster prevention and emergency response (+)	%	Suresh et al. (2024) and Zhuang, Wang, et al. (2024)
		Proportion of cumulative waterlogging mitigation investment	X6	Proportion of cumulative waterlogging mitigation investment in municipal infrastructure investment (+)	%	Hu and Wu (2024)
		Hospital beds per 10,000 people	X7	Number of hospital beds per 10,000 residents in each city (+)	beds/10,000 people	Chen et al. (2023) and Wang et al. (2024)
Redundancy	*c* (X14)	Labor productivity	X8	Economic output per unit of labor input in each city (+)	billion CNY / 10,000 people	Martin (2012) and Zhou and Qi (2023)
		Per capita road area	X9	Road area per person in each city (+)	m^2/person	Xu et al. (2024) and Zhang et al. (2023)
		Proportion of water-related personnel	X10	Proportion of urban employees in water, environment, and public facility management sectors (+)	%	Zhang et al. (2021)
		Proportion of land for logistics and warehousing	X11	Proportion of land allocated to logistics and warehousing in total urban construction land (+)	%	Aghajani et al. (2023) and Korucuk et al. (2024)
Resourcefulness	*d*	Fixed value = 1	/	Assumed full recovery to pre-disaster performance level (/)	/	Cassottana et al. (2019)

The (+) and (–) signs in the Description (attribute) column denote the indicator's mathematical correlation with the Function Parameter (for example, *a*, *b*, and *c*)

2.2.1 Robustness

Robustness emphasizes a city's inherent capacity to withstand extreme rainfall shocks and the quality of its defensive infrastructure, serving as the foundational dimension of resilience assessment. *Prep_shock* (X1) quantifies the economic sensitivity of urban systems to extreme rainfall, measured by the cumulative capital exposure at the grid level (%), following Cao et al. (2023). Equation 9 employs a spatiotemporal coupling method that integrates normalized rainfall intensity—filtered by a defined threshold (50 mm)—and the inverse of historical exceedance probability to construct a risk-weighted exposure index. This is further combined with the spatial distribution of fixed capital stock to achieve a multidimensional quantification of extreme rainfall impact intensity. A detailed explanation of the equation and its computational steps is provided in the Supplementary Material Section 3.[1]

It is crucial to clarify that *Prep_shock* is designed as a standardized measure of exposure to a hazard, not a direct measure of resilience itself. Our framework assesses resilience as a system's capacity to perform given this shock. The index is calculated systematically for all cities to provide a comparable shock magnitude, and its focus on "extreme" events is intentional. Only shocks that have the potential to overwhelm existing defensive capacities can provide a true test of a city's robustness attribute. Furthermore, by normalizing rainfall intensity against local historical patterns, the index ensures that the shock is evaluated relative to a city's specific climatic context, thus avoiding the pitfall of equating absolute rainfall with uniform impact.

2.2.2 Rapidity

Rapidity focuses on a city's emergency response efficiency and resource coordination capacity during extreme rainfall events, which directly influences the effectiveness of loss containment. Total factor productivity (X4) measures the technical efficiency of the urban economic system (%), reflecting the potential for optimal resource allocation during crisis (Tang et al. 2023). The proportion of fiscal expenditure on disaster prevention and emergency management (X5) captures the government's immediate response capacity through its share of emergency funding (%), as noted by Suresh et al. (2024). The proportion of cumulative fixed asset investment in waterlogging mitigation (X6) and the number of hospital beds per 10,000 people (X7) reflect, respectively, the pace of drainage infrastructure upgrades (%) and the spatial density of medical resources (beds per 10,000 people), both of which are essential for infrastructure repair and emergency healthcare during disasters (Chen et al. 2023; Hu and Wu 2024). These indicators form the backbone of the disaster-time response chain and help shorten the recovery period of system functions.

2.2.3 Redundancy

Redundancy reflects a city's capacity for resource buffering and functional substitution during the post-disaster recovery phase, serving as a critical component for enhancing long-term resilience. Labor productivity (X8), measured by economic output per unit of labor (billion CNY per 10,000 people), captures the capacity of human capital to support post-disaster reconstruction (Zhou and Qi 2023). Per capita road area (X9) serves as a proxy for transportation redundancy (m^2/person), facilitating the efficient movement of goods and evacuation of populations after a flood event (Zhang et al. 2023). The proportion of water-related personnel+ (X10) and the proportion of land allocated to logistics and warehousing (X11) represent, respectively, the reserve of professional personnel (%) and the redundancy of logistics nodes (%), both of which are essential for sustaining environmental management and material supply during recovery (Zhang et al. 2021; Korucuk et al. 2024). These multi-level redundancy indicators help reduce the duration of the disrupted state and enhance the stability of recovery trajectories.

$$Prep\_shock = \sum_{t=365}^{t_{shock}} \sum_{grid \in \Omega} \left(\underbrace{\frac{HR\_Intensity^{grid,t}}{Max\_Intensity^{grid,t}}}_{\text{Normalize intensity}} \times \underbrace{\frac{1}{Prob\_gte50^{grid}}}_{\text{Probability weight of historical rainstorm}} \times \underbrace{\frac{Capital\_shock^{grid,t}}{Capital^{city,t}}}_{\text{Capital stock exposure}} \right) \tag{9}$$

Drainage network density (X2) directly reflects the spatial coverage capacity of a city's drainage infrastructure (km/km^2), which determines the speed at which pluvial flood risks may spread (Li and Burian 2023). Proportion of cumulative fixed asset investment in flood control (X3) evaluates the long-term financial commitment to flood defense infrastructure (Liao et al. 2019). Together, these three indicators (X1, X2, and X3) capture the engineering defense capacity and economic system stability of a city under extreme rainfall, representing the first line of defense against disaster impacts.

2.3 Model of Attributing

To quantify the contribution of resilience parameters and indicators under extreme rainfall shocks, three machine learning models—random forest (RF) (Gu et al. 2025), explainable boosting machine (EBM) (Nori et al. 2019), and XGBoost (Li 2022; Liu et al. 2024; Zhang et al. 2025)—were trained and compared. These models are capable of capturing nonlinear relationships and interaction effects among resilience indicators while balancing predictive accuracy and interpretability. To ensure model generalization, hyperparameters were optimized using a random search strategy (Liu et al. 2024). Final model parameters were selected based on minimizing root mean square error (RMSE) on a 30% validation subset. The specific search space for each model's key hyperparameters and the final optimal values selected for predicting resilience and recovery time are detailed in the Supplementary Material (Table S2).[1] Detailed equations and procedures are provided in Supplementary Material Subsection 4.1.[1]

To uncover the driving mechanisms of urban resilience parameters under extreme rainfall shocks, this study adopts a multi-method framework to systematically quantify both main and interaction effects of resilience indicators. The SHAP values derived from the XGBoost model (Meddage et al. 2022) are used to analyze both global and instance-level contributions of each indicator, capturing underlying nonlinear relationships. Simultaneously, the inherently additive structure of the EBM (Nori et al. 2019) enables direct extraction of feature importance rankings, enhancing the interpretability and policy relevance of the results. To explore the dynamic coupling mechanisms among multidimensional resilience indicators, a three-level full factorial experimental design is employed (Smucker et al. 2019). Using analysis of variance (ANOVA), the framework identifies synergistic and antagonistic interactions among robustness, rapidity, and redundancy dimensions, as well as the directionality of these effects. This integrated approach balances predictive accuracy with interpretability, overcoming the limitations of conventional models in capturing high-order interactions. Furthermore, SHAP-based feature rankings and quantified interaction strengths provide an evidence-based foundation for prioritizing resilience optimization strategies under extreme rainfall scenarios. Detailed equations and procedures are available in Supplementary Material Subsection 4.2.[1]

2.4 Data sources

The data for this study cover the period 2019–2022. The majority of the data were sourced from official national publications, including the China Urban Construction Statistical Yearbook, the China Urban Statistical Yearbook, and the China Water Statistical Yearbook, which ensures standardized definitions and high cross-city consistency. The indicator for fiscal expenditure on disaster prevention (X5) was uniquely sourced from publicly available annual fiscal reports from individual city governments. Our final dataset was constructed by taking the intersection of all indicators; any city-year with missing data for any single indicator was excluded from the analysis. The temporal scope of the study was constrained by the availability of these official datasets. Daily historical rainfall data from 1 January 1961 to 31 December 2022, with a spatial resolution of 0.1° and a unit of mm/day, were provided by Han et al. (2023). To represent the exposure to extreme rainfall, we used gridded fixed capital stock as the impact target, based on 30-second resolution capital stock estimates for China in 2015, with units in million CNY (Wu et al. 2018). For a detailed breakdown of the source and access information for each indicator, please refer to Table S1 in the Supplementary Material.[1]

3 Results

This section presents the empirical findings of our study, organized in a multi-stage sequence. We begin by analyzing the spatiotemporal patterns of the extreme rainfall shock (*Prep_shock*) index and the resulting urban resilience across China from 2019 to 2022. We then examine the dynamics of urban recovery time and the shape of recovery trajectories. Following this, we introduce a diagnostic classification of cities based on their performance in a ternary parameter space, before finally delving into the attribution analysis to identify the key drivers of these observed patterns.

3.1 Extreme Rainfall Shock and Dynamic Resilience

To more accurately capture the regional extremity of rainfall shocks, we adjusted for spatial heterogeneity in rainfall distribution across China. As shown in Fig. 2a–d, the mean daily precipitation (*Prep_mean*) from 2019 to 2022 displayed a clear spatial gradient, with significantly higher precipitation levels in southeastern China compared to the northwest, reflecting substantial north-south disparities. Additionally, the probability of extreme rainfall events in northwestern China was extremely low. To eliminate this inherent climatic imbalance, we constructed an extreme rainfall impact index (*Prep_shock*) by integrating standardized rainfall intensity, capital exposure, and historical exceedance probability. For instance, 100 mm/day of rainfall may not be considered extreme in southern China, whereas the same amount in northern regions could constitute a severe event. A typical case is shown in Fig. 2h, which effectively quantifies the extreme severity of the once-in-a-millennium rainfall event that struck Henan Province in July 2021. This event

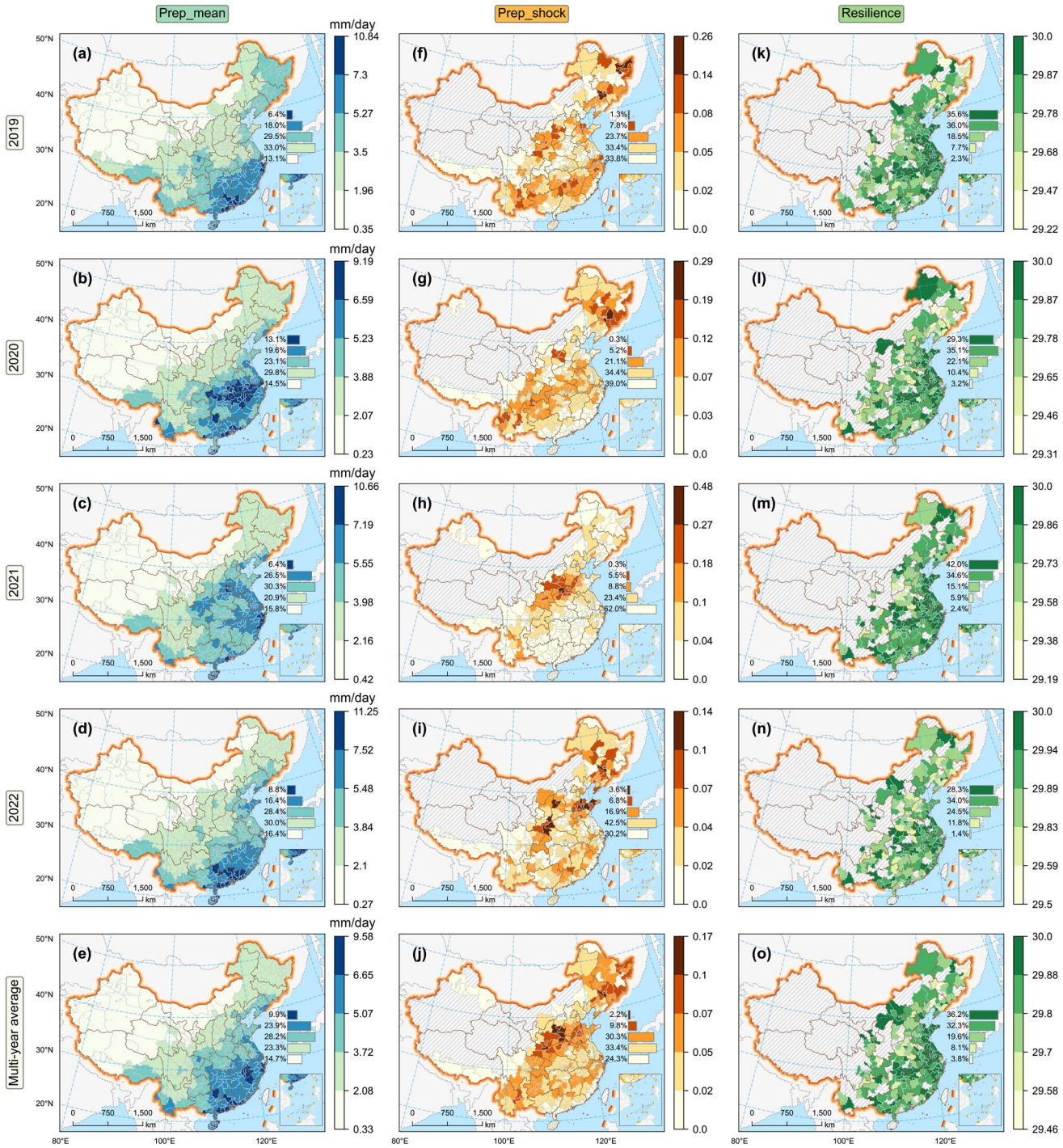

Fig. 2 Spatiotemporal distribution of mean daily precipitation, rainfall shock, and resilience from 2019 to 2022 and multi-year averages. The classification method is based on natural breaks (Jenks). **a–e** Spatial distribution of mean daily precipitation (*Prep_mean*) from 2019 to 2022 and the multi-year average (values are the mean daily precipitation in millimeters per day). **f–j** Spatial distribution of extreme rainfall shock (*Prep_shock*) from 2019 to 2022 and the multi-year average (values are the calculated unitless composite index scores). **k–o** Spatial distribution of resilience from 2019 to 2022 and the multi-year average. Percentage numbers show the proportion of cities falling into each class for the respective map. The hatched areas indicate missing data

serves as a powerful illustrative example of the index's ability to measure the magnitude of rare and catastrophic shocks. It is important to note, however, that a *Prep_shock* score was systematically calculated for every city in our sample to ensure a comprehensive and comparative assessment.

The spatial and temporal distribution of urban resilience in China from 2019 to 2022 remained generally stable, with most cities demonstrating strong resilience. As shown in Fig. S1,[1] only a small number of regions were affected by high-intensity rainfall events, while a large proportion of cities maintained high resilience levels. The multi-year average results indicate that 36.2% of cities fell into the highest resilience category (Fig. S1c[1]), predominantly located in eastern coastal areas (Fig. S2b[1]) such as Shandong Province and the Yangtze River Delta, followed by city clusters in the Pearl River Delta and the Beijing-Tianjin-Hebei region. In contrast, lower resilience levels were observed in parts of Henan Province and northeastern China. Notably, nine cities with the lowest resilience—accounting for 3.8% of the sample—were mostly concentrated in the northeast, specifically including Songyuan (Jilin Province), Shuangyashan and Hegang (Heilongjiang Province), Fuxin, Tieling, and Jinzhou (Liaoning Province), as well as Dazhou (Sichuan Province), Changzhi (Shanxi Province) and Shangqiu (Henan Province).

To further examine differences across city scales (Table S3[1]) and regions (Table S4[1]), we conducted a stratified analysis of urban classifications. The temporal analysis revealed that urban resilience fluctuated across all city sizes during the study period, with a general decline in 2020 before recovering in 2022. Megacities, in particular, exhibited a distinct temporal pattern of resilience to systemic shocks (Fig. S2a[1]). Consistent with conventional expectations, they demonstrated high resilience levels in 2019 and 2022, leveraging their superior resources and infrastructure. However, their resilience dropped sharply during the peak years of the COVID-19 pandemic (2020), falling below that of smaller cities. This temporary lack of resilience suggests that the systemic disruptions of the pandemic—such as strained fiscal resources and supply chain interruptions—may have uniquely hampered the capacity of these complex urban systems to manage concurrent extreme rainfall shocks.

3.2 Spatiotemporal Patterns of Urban Recovery Dynamics

Urban recovery time following extreme rainfall was estimated using recovery functions, with 30 days set as the upper limit. The results show that approximately 59.1% of cities were able to return to pre-disaster performance levels within 4.9 to 9.1 days, with these cities primarily located in Shandong, the Yangtze River Delta, Hubei, Hunan, and northern Jiangxi (Fig. 3f). In contrast, about 1.7% of cities—such as Xinyang in Henan Province (18.1 days), Lincang (21.7 days) and Zhaotong (21.7 days) in Yunnan Province, and Songyuan in Jilin Province (22.2 days)—required more than two weeks to recover. Notably, although Fig. 3g reveals substantial year-to-year differences in rainfall shock intensity, these differences did not result in corresponding fluctuations in recovery time. Instead, Figs. 3h–3i show that both recovery speed (parameter b) and redundancy (parameter c) remained stable over the four-year period, contributing to a generally steady and improving recovery trend. Specifically, the prolonged recovery time observed in southern Henan cities is less likely driven by variations in extreme rainfall shock (parameter a) and more plausibly associated with weaker recovery capacity or rapidity (b) and lower system redundancy (c).

To illustrate the recovery dynamics of cities with varying levels of recovery capacity, we applied the natural breaks (Jenks) classification method to divide the multi-year average recovery time into five levels, and selected one representative city from each level to visualize annual recovery curves (Figs. 3a–3e). A notable shortening of recovery time was observed in 2022. Cities with stronger recovery capacity—such as Zhoushan in Zhejiang Province (Fig. 3a), Ezhou in Hubei Province (Fig. 3b), Meizhou in Guangdong Province (Fig. 3c), and Nanchang in Jiangxi Province (Fig. 3d)—showed a steady decline in recovery time from 2020 to 2022. Even in Lincang, Yunnan Province (Fig. 3e), which had relatively weak recovery capacity, a marked improvement in recovery performance was evident by 2022.

Overall, the results suggest a general trend in which larger cities recover more quickly (Fig. S3[1]). However, similar to the resilience findings, megacities exhibited weaker recovery performance due to insufficient internal defense and recovery capacity to protect their highly concentrated capital assets (Fig. S3a[1]). Notably, recovery time peaked for megacities and large cities in 2020, while for other city size groups, the slowest recovery occurred in 2021. In terms of regional patterns, cities in the East region demonstrated significantly stronger recovery capacity compared to those in other regions, whereas cities in the Northwest and Southwest regions exhibited relatively low recovery performance (Fig. S3b[1]).

3.3 Diagnosis of Urban Resilience Based on Ternary Parameter Space

Figure 4 presents a ternary diagnostic analysis. Quadrant I cities exhibit strong recovery capacity (with greater recovery speed or rapidity) but weak shock intensity and redundancy. Quadrant II represents cities that rely primarily on high redundancy to recover, with low shock intensity and recovery capacity, and generally display strong resilience and short recovery times, demonstrating that their high redundancy is sufficient to compensate for their low recovery capacity. In contrast, Quadrant IV includes cities exposed to severe rainfall shocks with weak recovery and redundancy, highlighting urgent needs for resilience enhancement.

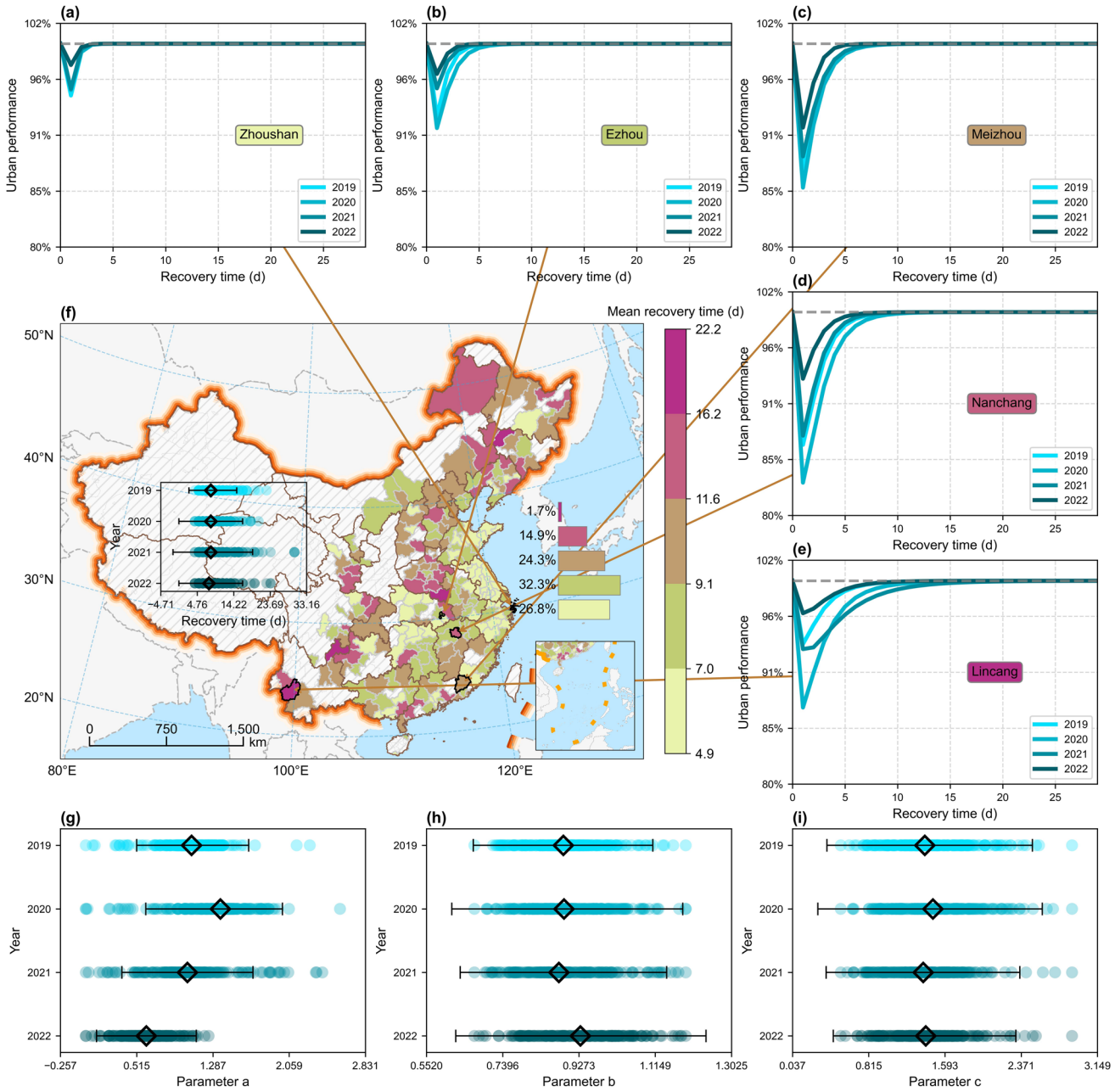

Fig. 3 Spatiotemporal distribution of recovery time and recovery trajectories of representative cities. **f** Spatial distribution of multi-year average recovery time, with the scatterplot on the left showing annual recovery time from 2019 to 2022. The percentage numbers show the proportion of cities falling into each class. **a**–**e** Recovery curves of five representative cities selected from the five classification levels in panel **f**, illustrating their recovery trajectories from 2019 to 2022. **g**–**i** Annual distributions of recovery function parameters *a*, *b*, and *c*. In the box plots, diamonds represent the medians, and the whiskers indicate the inner fences, defined as the maximum and minimum values within Q3 + 1.5 × IQR and Q1 − 1.5 × IQR, respectively. IQR is the interquartile range

Quadrant III cities account for the largest proportion across all years from 2019 to 2022 and in the multi-year average, reaching 75.6% (Fig. 4; Fig. S4[1]). In each year, large and medium-sized cities consistently made up the highest shares within this quadrant (Figs. S5a–S5d[1]), averaging 33.9% and 40.2%, respectively (Fig. S5e[1]). Geographically, these cities are primarily concentrated in the East and Central South regions, comprising 63.5% of the total (Fig. S6e[1]). Given their relatively balanced performance and moderate exposure, these cities do not require substantial policy intervention.

The megacities in our study are primarily found in Quadrants I and III. Multi-year averages show that Shanghai and Guangzhou serve as recovery-capacity exemplars, while

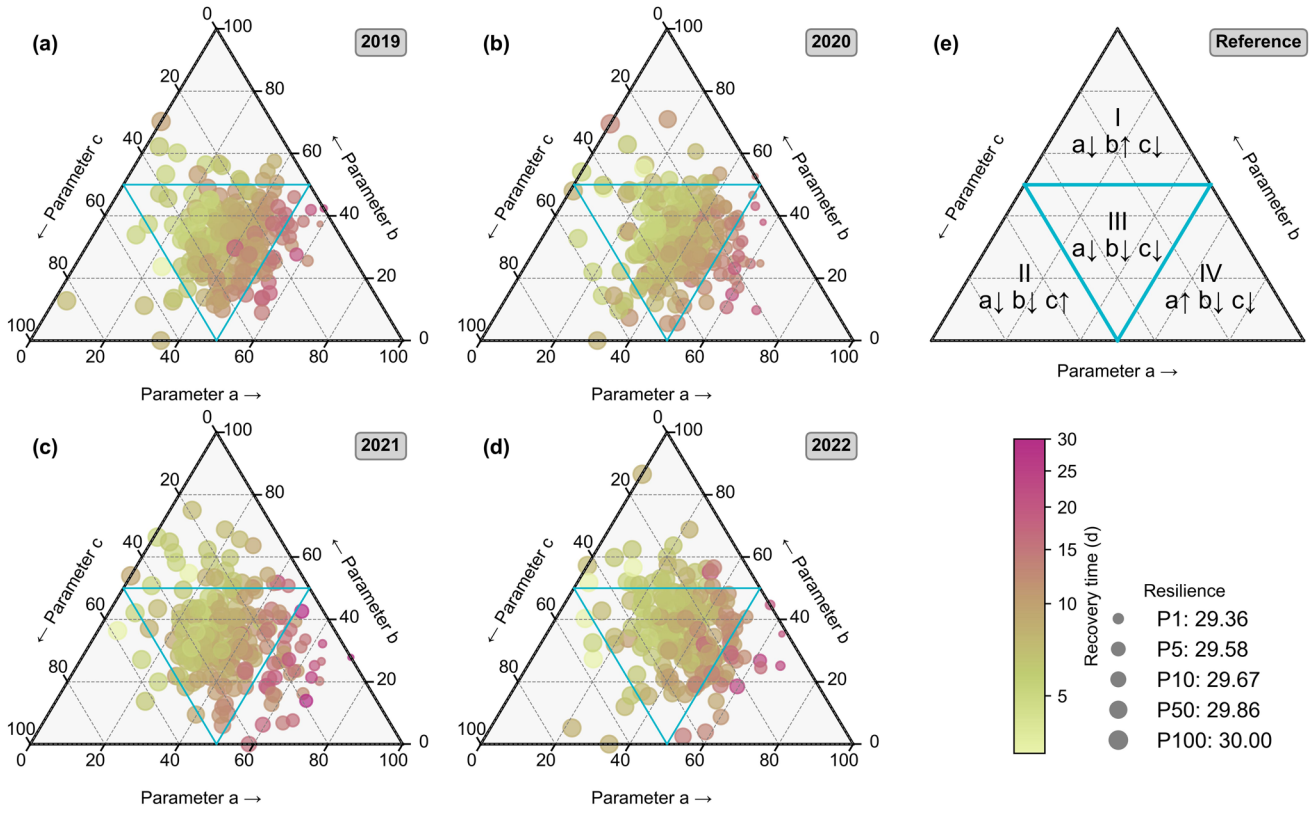

Fig. 4 Ternary scatter plots of resilience parameters from 2019 to 2022. **a**–**d** Annual ternary plots of city-level resilience parameters from 2019 to 2022. Dot size represents the magnitude of resilience, and color indicates recovery time. **e** Quadrant classification reference based on the three parameters. Arrows indicate relative magnitude: ↑ denotes values above 50 (high level), ↓ denotes values below 50 (low level)

Beijing, Chongqing, and Tianjin fall into Quadrant III (Fig. S4[1]). Representative cities in Quadrant I are predominantly large cities (Fig. S5e[1]), mostly located in the East and Central South regions (Fig. S6e[1]). In contrast, representative cities in Quadrant II are typically small cities, mainly distributed across the North and Central South (Fig. S6e[1]). These findings suggest that large cities tend to possess stronger recovery capacity, whereas small cities are more adept at leveraging substitution mechanisms for recovery.

Problem diagnosis suggests that cities in Quadrant IV should urgently improve their resilience levels. Although this group is primarily composed of medium-sized cities (39.1%) and small cities (47.8%) (Fig. S5e[1]), mainly located in the North and Central South regions, it is noteworthy that two super large cities—Kunming in Yunnan Province (2020) and Zhengzhou in Henan Province (2021)—also fell into Quadrant IV. This indicates that both cities require greater emphasis on enhancing resilience to extreme rainfall shocks. Moreover, among the nine low-resilience cities identified in Fig. 2 and the four cities with the longest recovery times in Fig. 3, nearly all are located within Quadrant IV (Table S5[1]).

3.4 Attribution Analysis

Having established the spatiotemporal patterns of resilience and recovery, this subsection delves into the underlying drivers of these outcomes. The analysis begins by comparing the predictive performance of the three machine learning models (RF, EBM, and XGBoost) to identify the most suitable models for our dataset. Subsequently, using the insights from the best-performing models, we analyze the main effects of each indicator and explore the complex, nonlinear interaction effects among key factors and parameters that govern urban resilience and recovery time.

3.4.1 Performance of Machine Learning Models

We compared the performance of RF, EBM, and XGBoost in predicting both resilience and recovery time, using evaluation metrics including mean squared error (MSE), root mean square error (RMSE), mean absolute error (MAE), and coefficient of determination (R^2). On the test set, XGBoost achieved the best performance for resilience prediction, with the lowest MSE (~0.133), RMSE (~0.365), and an R^2 of approximately 0.87. In contrast, EBM demonstrated superior

generalization ability for recovery time prediction, achieving a test-set MSE of ~0.035, RMSE of ~0.187, and an R^2 close to 0.97 (Fig. 5). Notably, this pattern of performance differentiation was consistent across both training and test sets, suggesting that EBM is more effective in capturing the complex patterns underlying recovery time, while XGBoost performs better in modeling resilience.

The performance of RF was comparatively weaker than that of the other two models. This can be attributed to differences in algorithmic design: while both EBM and XGBoost employ a boosting approach, RF is based on bagging. Boosting models like EBM and XGBoost iteratively fit residuals and leverage flexible regularization and hyperparameter tuning strategies, enabling them to capture more complex nonlinear patterns. As a result, they tend to achieve higher accuracy and more stable generalization performance in modeling the intricate dynamics of urban resilience and recovery processes.

3.4.2 Main Effects and Interaction Effects Analysis

X14 (parameter *c*) emerged as the most influential factor in both resilience and recovery time predictions (Fig. 6c, f). Therefore, redundancy design plays a critical role in enhancing system robustness by providing alternative resources or backup pathways when localized functions are disrupted. Such design can effectively mitigate the impact of vulnerable components on overall system performance and significantly reduce the time required for reconstruction or repair. The rankings of key factors across different models show a considerable degree of mutual consistency, reinforcing the reliability of the findings.

For resilience, besides X14, X12 (parameter *a*, an inverse measure of robustness) and X9 (per capita road area) had a strong positive impact (Fig. 6c). For recovery time, X13 (parameter *b*, recovery speed) and X9 were also important, while X12 had little effect (Fig. 6f). These results align with Fig. 3, showing that robustness mainly affects resilience, while faster recovery depends more on emergency support (for example, hospital beds density and fiscal inputs) and redundant infrastructure (for example, road density).

To ensure the robustness of our feature importance findings and address potential multicollinearity, which can affect the interpretation of attribution models, we conducted additional diagnostic tests before analyzing the main effects. A variance inflation factor (VIF) analysis was performed on all predictor variables, confirming that multicollinearity was not a significant issue. Furthermore, a permutation feature importance analysis was conducted on the best-performing models to provide a more robust, alternative assessment of feature importance. Both analyses confirmed that the results presented here are reliable and not statistical artifacts. The detailed results of these diagnostic tests are provided in the Supplementary Material (see Tables S8, S9, and S10).[1]

In the three-level factorial experiment involving three parameters, second-order interaction effects were not

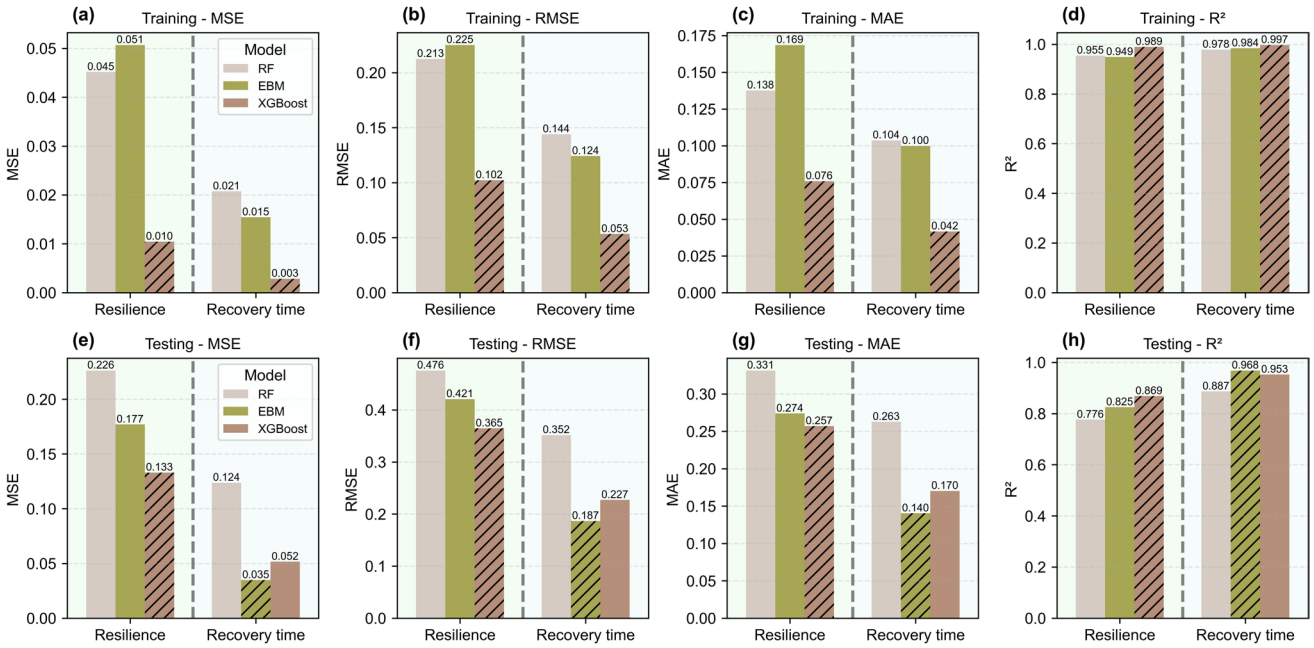

Fig. 5 Comparison of model performance across random forest (RF), explainable boosting machine (EBM), and extreme gradient boosting (XGBoost). **a**–**d** Model performance on the training set. **e**–**h** Model performance on the test set. *MSE* Mean squared error, *RMSE* Root mean square error, *MAE* Mean absolute error, R^2 Coefficient of determination. The shaded bars represent the best-performing models

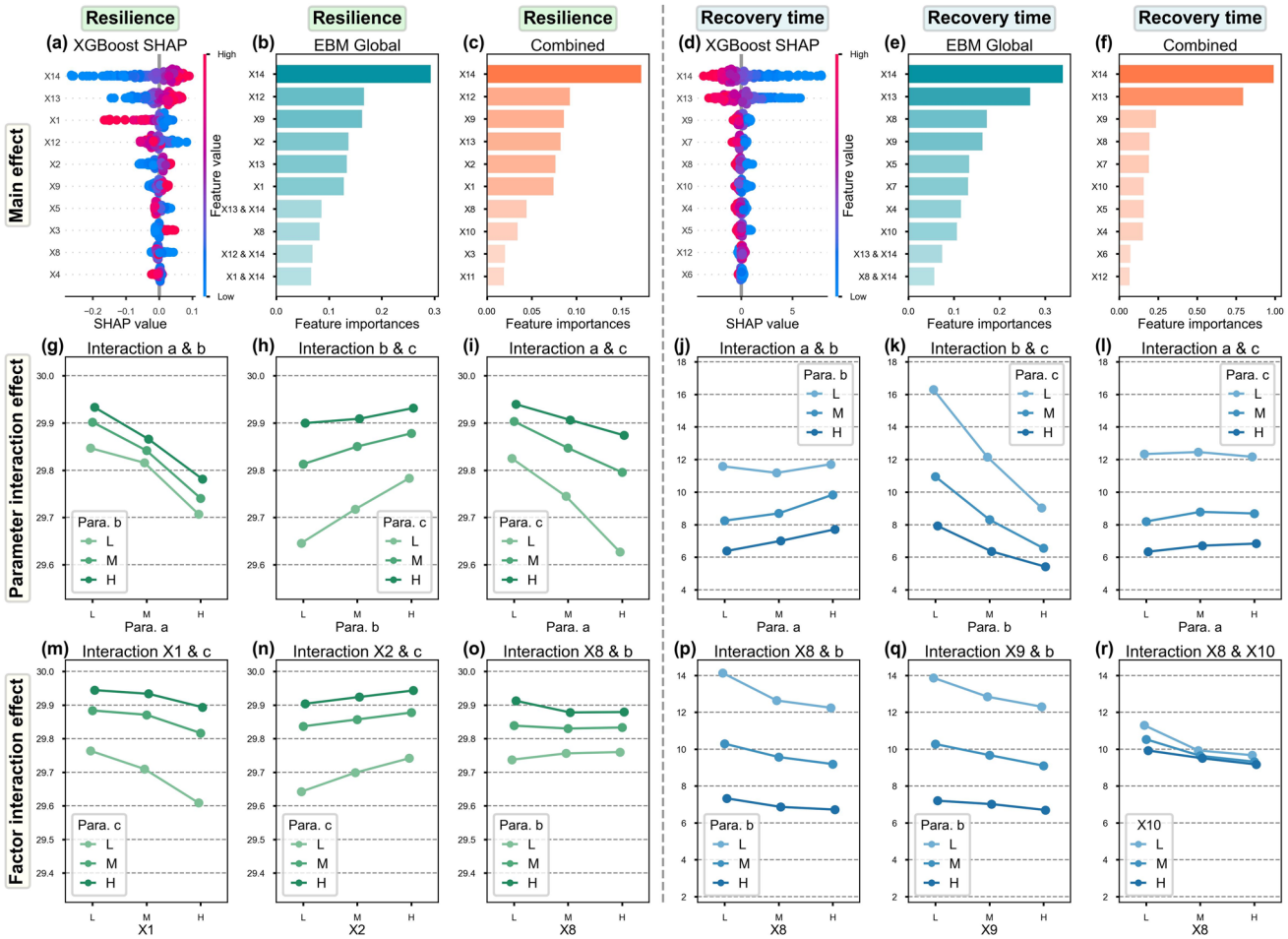

Fig. 6 Analysis of the main and interaction effects of parameters and factors on resilience and recovery time. **a**–**f** Main effect analysis of parameters and factors. X12–X14 represent parameters *a*, *b*, and *c*, respectively. **a** and **d** are SHAP-based attribution results from the XGBoost model, **b** and **e** are intrinsic global explanations from the EBM model, and **c** and **f** are combined insights from both models. **g**–**l** First-order interaction parameter plots for *a*, *b*, and *c* derived from the three-level full factorial experiments. **m**–**r** First-order interaction plots for factors X1–X14, based on the 3^{14} full factorial simulation. The plots display the top three pairwise interaction effects for each of the 14 factors. L, M, and H represent low, medium, and high levels

significant, so the analysis focused on first-order interactions between parameters *a*–*b*, *b*–*c*, and *a*–*c* (Fig. 6g–l). For resilience, the *a*–*b* interaction (Fig. 6g) showed a weak negative synergy (antagonism) (P = 0.0260, Table S6[1]). Specifically, the positive contribution of increasing recovery speed (*b*) to resilience was most significant at low levels of shock intensity (*a*), but this beneficial effect was substantially weakened (that is, the slope of the interaction line became flatter) as shock intensity (*a*) increased. The *b*–*c* interaction (Fig. 6h) was a positive antagonism: as redundancy (*c*) increased, the marginal benefit of increasing *b* diminished (P = 0.0000). The *a*–*c* interaction (Fig. 6i) showed negative antagonism, with higher *c* values weakening the negative impact of *a* (P = 0.0000). For recovery time, the *a*–*b* interaction (Fig. 6j) also showed a significant and complex negative synergy (antagonism) (P = 0.0008, Table S7[1]). The analysis of the interaction plot reveals a nonlinear relationship: at the low level of recovery speed (Para. *b* = L), increasing shock intensity (*a*) from L to M is associated with a slight reduction in recovery time, before increasing again from M to H, indicating a turning point. In contrast, at medium and high levels of recovery speed (Para. *b* = M and H), increasing shock intensity (*a*) consistently and significantly lengthens (worsens) the recovery time. The *b*–*c* interaction (Fig. 6k) exhibited positive antagonism, where higher *c* reduced the marginal impact of *b* (P = 0), while the *a*–*c* interaction was not significant (Fig. 6l). Among all interactions, the *a*–*c* interaction had the most significant effect on resilience, suggesting that enhancing redundancy is particularly effective under high-impact rainfall conditions. In contrast, *b*–*c* was the dominant interaction for recovery time, indicating that simultaneous improvements in recovery speed and redundancy may offset each other's benefits. These non-parallel interaction trends

highlight the critical role of parameter coupling in shaping both resilience and recovery outcomes.

To further investigate the interactions between factors and parameters, we selected the 5th, 50th, and 95th percentiles of each indicator as three experimental levels, and used the best-performing model to predict the full factorial combinations of all 14 factors (3^{14} = 4,782,969 simulations). For resilience, the results show that when urban economic impact of extreme rainfall (X1) increases, a higher value of parameter *c* (redundancy) can effectively buffer the decline in resilience (Fig. 6m), consistent with the findings in Fig. 6i**.** Enhancing drainage network density (X2) is more effective when *c* is low (Fig. 6n), while improving labor productivity (X8) has a greater impact on resilience when recovery speed (*b*) is low (Fig. 6o). For recovery time, both labor productivity and per capita road area (X9) significantly accelerate recovery when *b* is at a low level (Figs. 6p and 6q). Additionally, the effect of labor productivity (X8) is further amplified when the share of water-related personnel (X10) is low (Fig. 6r). These results reveal how different factors regulate system resilience and recovery dynamics under varying parameter conditions, underscoring the importance of context-specific adjustments in resilience optimization strategies.

4 Discussion

Our study provides a dynamic assessment of urban resilience to extreme rainfall, revealing nuanced spatial patterns and complex driver interactions. The findings both align with and challenge existing theories, offering new insights for urban resilience planning.

4.1 Interpretation of Key Findings

Our attribution analysis consistently identified redundancy as the most dominant attribute for enhancing resilience and shortening recovery time. This finding aligns with complex systems theory (Rinaldi et al. 2001), which posits that redundant systems with substitutable components are less vulnerable to cascading failures—a critical feature during extreme floods when primary infrastructure nodes (for example, power stations, transport hubs) are likely to be compromised (Buldyrev et al. 2010). The high importance of indicators like per capita road area (X9) (Ma et al. 2023) and land for logistics (X11) (Aghajani et al. 2023) underscores that physical redundancy in transportation and supply chains is paramount for facilitating emergency response and post-disaster reconstruction.

A particularly noteworthy finding is the observed temporal decline in the resilience of megacities during the COVID-19 pandemic. While these urban giants demonstrated high resilience in 2019 and 2022 (Fig. S2a[1]), aligning with expectations, their calculated resilience dropped sharply in 2020–2021. This suggests a heightened sensitivity of these complex systems to the compound effects of the systemic (pandemic) and localized (rainfall) shocks occurring concurrently. Conceptually, vulnerability refers to a system's susceptibility to initial impact, whereas resilience is the overall outcome encompassing resistance and recovery. This observed temporal decline suggests that megacities' intrinsic vulnerability (for example, infrastructure susceptibility) did not necessarily increase during 2020–2021. A more plausible explanation, consistent with resilience theory, is that the pandemic acted as a systemic shock that temporarily compromised their overall resilience capacities—particularly the ability to mobilize resources for effective recovery (conceptually related to rapidity and redundancy). Consequently, this reduction in capacity likely led to the observed poorer performance (lower calculated resilience scores) when these cities faced concurrent extreme rainfall hazards during those specific years. This finding aligns with recent studies suggesting nonlinear impacts from compound crises in complex urban systems (Sadler et al. 2024).

Furthermore, our ternary analysis revealed that many small cities fall into Quadrant II, characterized by high redundancy but low internal recovery capacity (rapidity). While our study did not measure inter-city connectivity directly, this finding suggests a plausible hypothesis grounded in regional resilience theory. The resilience of smaller urban areas may not stem from internal self-sufficiency, but rather from their functional connectivity to larger, neighboring cities. Their high "redundancy" could reflect their ability to draw upon external resources—such as emergency supplies, specialized personnel, and economic support—from a wider metropolitan region, compensating for their limited internal response capacity (Bai 2024; Yao et al. 2025).

4.2 The Trade-off Between Rapidity and Redundancy

Our factorial experiments uncovered a positive antagonistic interaction between recovery speed or rapidity (*b*) and redundancy (*c*), suggesting that simultaneous improvements in both may lead to diminishing marginal returns. This counter-intuitive finding can be explained by considering the potential for "coordination friction" between different types of resilience strategies currently being implemented in China: centralized, high-tech systems for rapidity, and decentralized, nature-based systems for redundancy.

A prime example of a rapidity-focused strategy is the development of Smart City platforms or City Brains, as seen in cities like Shanghai (Zhu et al. 2024) and Hangzhou (Bai et al. 2025). These platforms use vast networks of Internet

of Things (IoT) sensors, artificial intelligence (AI), and centralized command centers to achieve real-time monitoring and highly efficient, rapid emergency response. For flood management, a City Brain can process data from water level sensors and weather forecasts to optimize the operation of massive centralized pumps and floodgates with great speed (Luusua et al. 2023).

Conversely, the Sponge City initiative, implemented in over 30 cities including Wuhan and Xiamen, is a quintessential redundancy-focused strategy (Yin et al. 2021). It relies on decentralized, nature-based solutions—such as permeable pavements, green roofs, and retention ponds—to create a redundant network that absorbs and manages rainwater at its source, reducing the load on the primary "gray" drainage infrastructure (Liu and Jensen 2018).

The potential trade-off emerges at the intersection of these two strategies. A high-tech City Brain (rapidity) is typically optimized to control the predictable, engineered "gray" infrastructure. However, during a catastrophic flood that overwhelms the primary system, its effectiveness depends on leveraging the thousands of decentralized Sponge City assets. If the real-time performance data from these green infrastructure elements (for example, soil saturation levels, local ponding) is not fully integrated into the City Brain's AI decision-making models, a coordination friction can occur. The command center might efficiently manage its centralized pumps, while being unable to account for the variable, localized performance of the decentralized sponge network. This could lead to suboptimal decisions, such as dispatching resources to an area where sponge infrastructure is already effectively mitigating the flood, while neglecting another area where it is failing. This illustrates that resilience strategies must be coherently integrated; investments in high-tech rapidity and distributed redundancy must be synergistic to avoid operating in parallel, potentially conflicting, silos.

4.3 Policy Implications and the Diagnostic Framework

The primary practical contribution of this study is the four-quadrant diagnostic framework, which supports the development of targeted, cost-effective resilience strategies (Table 2). For cities in Quadrant IV (for example, Zhengzhou in 2021), characterized by high shock intensity and low recovery capacity/redundancy, the immediate priority should be enhancing redundant systems. In contrast, cities in Quadrant II, which already possess high redundancy, should focus on improving their emergency response efficiency (rapidity), with investments in human capital (for example, labor productivity) being a key lever. This tailored approach moves beyond one-size-fits-all policies and provides a data-driven tool for municipal governments to prioritize investments based on their specific resilience profile.

Table 2 Differentiated optimal strategies for urban resilience enhancement

Urban quadrant	Diagnostic characteristics	Representative cities	Recommended resilience strategy
IV	High rainfall shock intensity; low recovery capacity and redundancy	Songyuan, Shuangyashan, Fuxin, Tieling, Jinzhou, Changzhi, Shangqiu, Lincang, Xinyang, Zhaotong	Prioritize enhancing redundancy, considering cost-effectiveness in resource allocation.
I	Low rainfall shock; high recovery capacity; low redundancy	Zhuhai, Zunyi, Wuxi, Taizhou, Zhongshan, Zhoushan, Jinhua, Huzhou, Liaoyang, Shanghai, Guangzhou, Yichun, Qitaihe, Foshan, Dongguan	Recovery capacity is well developed; focus on improving redundancy, especially through expanding drainage network density.
II	Low rainfall shock; low recovery capacity; high redundancy	Baotou, Sanya, Beihai, Ordos, Zhongwei, Chuzhou, Fangchenggang, Ulanqab	Redundancy is sufficient; priority should be given to enhancing recovery speed, with labor productivity as a key lever.
III	Low rainfall shock; low recovery capacity and redundancy	Remaining cities	Given the low likelihood of extreme rainfall, substantial policy intervention is not required.

4.4 Limitations and Future Research

This study has several limitations that open avenues for future research. First, a key limitation is the assumption of constant resourcefulness (parameter $d = 1$). This attribute, which includes crucial elements like governance capacity and early warning systems, is conceptually complex and notoriously difficult to quantify with standardized data across a large and diverse sample of cities. Due to the lack of consistent national-level data for these factors, we adopted the pragmatic assumption of full recovery to enable a robust quantitative comparison. However, to test the robustness of our core findings against this necessary simplification, we performed a comprehensive sensitivity analysis. The results, detailed in the Supplementary Material (Subsection 10.1),[1] show that the relative resilience and recovery time rankings of the cities remain highly stable even when the d parameter is varied. This provides strong evidence that our main conclusions regarding spatial patterns and key drivers are not artifacts of this assumption. Future research should aim to overcome this limitation, perhaps through in-depth qualitative case studies or the development of novel data sources to explore how dynamic resourcefulness shapes recovery. The modeling choices, including the adoption of a gamma-based recovery function and a fixed 30-day integration boundary, are also potential limitations. To address this, a comprehensive sensitivity analysis was performed. The results, detailed in the Supplementary Material (Subsections 10.2 and 10.3),[1] demonstrate that the study's primary conclusions regarding the relative resilience of cities are highly robust to variations in both the time boundary and the specific functional form used. This provides strong confidence in the stability of our findings.

Second, the study period of 2019–2022, while capturing a critical period of intense rainfall events and systemic shocks, was constrained by the availability of consistent official data, particularly for fiscal expenditures. Future research should expand the temporal scope of this dynamic analysis as more years of data become publicly available, which would allow for the examination of longer-term resilience trends and policy impacts.

Finally, verifying the hypothesis regarding the role of inter-city connectivity for smaller cities presents a valuable direction for future work. This would require the integration of regional network, transportation flow, and economic linkage data to explicitly model how regional redundancy contributes to the resilience of individual urban areas.

5 Conclusion

This study proposed and validated a dynamic framework for assessing and optimizing urban resilience to extreme rainfall by integrating interpretable machine learning and factorial experiments. Based on an analysis of over 220 Chinese cities from 2019 to 2022, four key conclusions emerged:

1. The novel *Prep_shock* index successfully normalizes for regional climatic disparities, providing a more accurate and equitable measure of extreme rainfall shock. This methodological advance enables the identification of true resilience patterns, revealing high-resilience city clusters in eastern coastal China and low resilience in regions like Henan Province (Fig. 2).
2. Urban resilience exhibits significant temporal dynamics, with megacities showing a unique vulnerability to the compound shock of the COVID-19 pandemic. While highly resilient in normal years, their performance dropped sharply in 2020, highlighting the challenges that systemic disruptions pose to complex urban systems (Fig. S2a[1]).
3. Redundancy is unambiguously identified as the most dominant attribute driving both higher resilience and faster recovery. Attribution analysis consistently shows that indicators of redundant infrastructure and resources are the most critical factors, far outweighing others. Factorial experiments further reveal complex interaction effects, such as the trade-off between simultaneously enhancing rapidity and redundancy, which underscores the need for context-specific optimization (Fig. 6).
4. The proposed four-quadrant diagnostic framework provides a powerful tool for policy making. By classifying cities based on their resilience attribute profiles, it enables the formulation of targeted and cost-effective resilience strategies, moving beyond one-size-fits-all approaches and offering a practical guide for urban planners and managers (Fig. 4; Table 2).

Acknowledgments This work was supported by the National Key R&D Program of China (Grant No. 2024YFC3014100), the National Natural Science Foundation of China (Grant No. 52394232), the General Program of National Natural Science Foundation of China (Grant No. 42377467), and the Fundamental Research Funds for the Central Universities (Grant No. 2243300007).

References

Aghajani, M., S. Ali Torabi, and N. Altay. 2023. Resilient relief supply planning using an integrated procurement-warehousing model under supply disruption. *Omega* 118: Article 102871.

Bai, X. 2024. Build networked resilience across cities. *Science* 383(6687): Article eado5304.

Bai, O., Y. Shi, and F. Wu. 2025. Pioneering the post-smart cities paradigm in urban innovation ecosystems governance: A case study of Hangzhou City-Brain Initiative. *Urban Policy and Research* 43(3): 260–284.

Berke, P.R., and T.J. Campanella. 2006. Planning for postdisaster resiliency. *The Annals of the American Academy of Political and Social Science* 604(1): 192–207.

Box, G., S. Hunter, and W. Hunter. 2005. *Statistics for experimenters: Design, innovation, and discovery*, 2nd edn. Hoboken, NJ: John Wiley & Sons Inc.

Bruneau, M., S.E. Chang, R.T. Eguchi, G.C. Lee, T.D. O'Rourke, A.M. Reinhorn, M. Shinozuka, and K. Tierney et al. 2003. A framework to quantitatively assess and enhance the seismic resilience of communities. *Earthquake Spectra* 19(4): 733–752.

Buldyrev, S.V., R. Parshani, G. Paul, H.E. Stanley, and S. Havlin. 2010. Catastrophic cascade of failures in interdependent networks. *Nature* 464(7291): 1025–1028.

Cao, L. 2023. AI and data science for smart emergency, crisis and disaster resilience. *International Journal of Data Science and Analytics* 15(3): 231–246.

Cao, F., X. Xu, C. Zhang, and W. Kong. 2023. Evaluation of urban flood resilience and its space-time evolution: A case study of Zhejiang Province, China. *Ecological Indicators* 154: Article 110643.

Cassottana, B., L. Shen, and L.C. Tang. 2019. Modeling the recovery process: A key dimension of resilience. *Reliability Engineering & System Safety* 190: Article 106528.

Chelleri, L., J.J. Waters, M. Olazabal, and G. Minucci. 2015. Resilience trade-offs: Addressing multiple scales and temporal aspects of urban resilience. *Environment and Urbanization* 27(1): 181–198.

Chen, X., L. Yu, W. Lin, F. Yang, Y. Li, J. Tao, and S. Cheng. 2023. Urban resilience assessment from the multidimensional perspective using dynamic Bayesian network: A case study of Fujian Province, China. *Reliability Engineering & System Safety* 238: Article 109469.

Cutter, S.L., L. Barnes, M. Berry, C. Burton, E. Evans, E. Tate, and J. Webb. 2008. A place-based model for understanding community resilience to natural disasters. *Global Environmental Change* 18(4): 598–606.

Diakoulaki, D., G. Mavrotas, and L. Papayannakis. 1995. Determining objective weights in multiple criteria problems: The CRITIC method. *Computers & Operations Research* 22(7): 763–770.

Folke, C. 2006. Resilience: The emergence of a perspective for social-ecological systems analyses. *Global Environmental Change* 16(3): 253–267.

Gilmore, E.A., C. Kousky, and T.S. Clair. 2022. Climate change will increase local government fiscal stress in the United States. *Nature Climate Change* 12(3): 216–218.

Gu, T., H. Zhao, L. Yue, J. Guo, Q. Cui, J. Tang, Z. Gong, and P. Zhao. 2025. Attribution analysis of urban social resilience differences under rainstorm disaster impact: Insights from interpretable spatial machine learning framework. *Sustainable Cities and Society* 118: Article 106029.

Gunderson, L., and C.S. Holling. 2002. *Panarchy: Understanding transformations in human and natural systems*. Fort Lauderdale, FL: Island Press.

Han, H., X. Bai, R. Costanza, and L. Dong. 2024. The effects of Covid-19 on the resilience of urban life in China. *npj Urban Sustainability* 4(1): Article 32.

Han, J., C. Miao, J. Gou, H. Zheng, Q. Zhang, and X. Guo. 2023. A new daily gridded precipitation dataset for the Chinese mainland based on gauge observations. *Earth System Science Data* 15(7): 3147–3161.

Hemmati, M., K. Kornhuber, and A. Kruczkiewicz. 2022. Enhanced urban adaptation efforts needed to counter rising extreme rainfall risks. *npj Urban Sustainability* 2(1): Article 16.

Holling, C.S. 1973. Resilience and stability of ecological systems. *Annual Review of Ecology and Systematics* 4(1): 1–23.

Holling, C.S. 1996. *Engineering resilience versus ecological resilience*. Washington, DC: National Academies Press.

Hosseini, S., K. Barker, and J.E. Ramirez-Marquez. 2016. A review of definitions and measures of system resilience. *Reliability Engineering & System Safety* 145: 47–61.

Hu, T., and J. Wu. 2024. Shaping the general resilience of green infrastructure through integrating structures, functions, and connections. *Journal of Environmental Management* 369: Article 122294.

Khoshkonesh, A., R. Nazari, M.R. Nikoo, and M. Karimi. 2024. Enhancing flood risk assessment in urban areas by integrating hydrodynamic models and machine learning techniques. *Science of the Total Environment* 952: Article 175859.

Klise, K.A. 2023. Increasing resilience with wastewater reuse. *Nature Water* 1(12): 1002–1003.

Korucuk, S., A. Aytekin, Ö. Görçün, V. Simic, and Ö. Faruk Görçün. 2024. Warehouse site selection for humanitarian relief organizations using an interval-valued Fermatean fuzzy LOPCOW-RAFSI model. *Computers & Industrial Engineering* 192: Article 110160.

Kotz, M., A. Levermann, and L. Wenz. 2022. The effect of rainfall changes on economic production. *Nature* 601(7892): 223–227.

Laidlaw, S., and S. Percival. 2024. Flood resilience: A review of evolving definitions. *Natural Hazards* 120(12): 10773–10784.

Li, Z. 2022. Extracting spatial effects from machine learning model using local interpretation method: An example of SHAP and XGBoost. *Computers, Environment and Urban Systems* 96: Article 101845.

Li, J., and S.J. Burian. 2023. Evaluating real-time control of stormwater drainage network and green stormwater infrastructure for enhancing flooding resilience under future rainfall projections. *Resources, Conservation and Recycling* 198: Article 107123.

Li, H., F. Deuser, W. Yin, X. Luo, P. Walther, G. Mai, W. Huang, and M. Werner. 2025. Cross-view geolocalization and disaster mapping with street-view and VHR satellite imagery: A case study of hurricane Ian. *ISPRS Journal of Photogrammetry and Remote Sensing* 220: 841–854.

Li, Z., Z. Zhou, H. Wang, X. Li, X. Shi, J. Xiao, Z. Yang, M. Sun, et al. 2025. Artificial intelligence-incorporated prediction for urban flooding processes in the past 20 years: A critical review. *Environmental Modelling & Software* 192: Article 106525.

Liao, K.-H., J.K.H. Chan, and Y.-L. Huang. 2019. Environmental justice and flood prevention: The moral cost of floodwater redistribution. *Landscape and Urban Planning* 189: 36–45.

Liu, L., and M.B. Jensen. 2018. Green infrastructure for sustainable urban water management: Practices of five forerunner cities. *Cities* 74: 126–133.

Liu, Q., J. Wang, and B. Bai. 2024. Unveiling nonlinear effects of built environment attributes on urban heat resilience using interpretable machine learning. *Urban Climate* 56: Article 102046.

Liu, X., X. Zhang, R. Ren, and H.N. Mahmoud. 2025. Assessment of China's 20 years of infrastructure and policy development for flood disaster management. *International Journal of Disaster Risk Reduction* 117: Article 105211.

Lundberg, S.M., and S.-I. Lee. 2017. *A unified approach to interpreting model predictions*. Red Hook, NY: Curran Associates Inc.

Luusua, A., J. Ylipulli, M. Foth, and A. Aurigi. 2023. Urban AI: Understanding the emerging role of artificial intelligence in smart cities. *AI & Society* 38(3): 1039–1044.

Ma, F., Y. Ao, X. Wang, H. He, Q. Liu, D. Yang, and H. Gou. 2023. Assessing and enhancing urban road network resilience under rainstorm waterlogging disasters. *Transportation Research Part D-Transport and Environment* 123: Article 103928.

Martin, R. 2012. Regional economic resilience, hysteresis and recessionary shocks. *Journal of Economic Geography* 12(1): 1–32.

McClymont, K., D. Morrison, L. Beevers, and E. Carmen. 2020. Flood resilience: A systematic review. *Journal of Environmental Planning and Management* 63(7): 1151–1176.

Meddage, D.P.P., I.U. Ekanayake, A.U. Weerasuriya, C.S. Lewangamage, K.T. Tse, T.P. Miyanawala, and C.D.E. Ramanayaka. 2022. Explainable machine learning (XML) to predict external wind pressure of a low-rise building in urban-like settings. *Journal of Wind Engineering and Industrial Aerodynamics* 226: Article 105027.

Meerow, S., and J.P. Newell. 2019. Urban resilience for whom, what, when, where, and why?. *Urban Geography* 40(3): 309–329.

Meerow, S., J.P. Newell, and M. Stults. 2016. Defining urban resilience: A review. *Landscape and Urban Planning* 147: 38–49.

Moghadas, M., A. Asadzadeh, A. Vafeidis, A. Fekete, and T. Kötter. 2019. A multi-criteria approach for assessing urban flood resilience in Tehran, Iran. *International Journal of Disaster Risk Reduction* 35: Article 101069.

Nori, H., S. Jenkins, P. Koch, and R. Caruana. 2019. InterpretML: A unified framework for machine learning interpretability. arXiv: 1909.09223.

Ouyang, M., and L. Dueñas-Osorio. 2014. Multi-dimensional hurricane resilience assessment of electric power systems. *Structural Safety* 48: 15–24.

Qian, J., Y. Du, F. Liang, J. Yi, X. Zhang, J. Jiang, N. Wang, W. Tu, et al. 2024. Measuring community resilience inequality to inland flooding using location aware big data. *Cities* 149: Article 104915.

Qin, X., S. Wang, M. Meng, H. Long, H. Zhang, and H. Shi. 2025. Enhancing urban resilience through machine learning-supported flood risk assessment: Integrating flood susceptibility with building function vulnerability. *npj Urban Sustainability* 5(1): 1–19.

Rinaldi, S.M., J.P. Peerenboom, and T.K. Kelly. 2001. Identifying, understanding, and analyzing critical infrastructure interdependencies. *IEEE Control Systems Magazine* 21(6): 11–25.

Rose, A. 2007. Economic resilience to natural and man-made disasters: Multidisciplinary origins and contextual dimensions. *Environmental Hazards* 7(4): 383–398.

Sadler, A., N. Ranger, S. Fankhauser, F. Marotta, and B. O'Callaghan. 2024. The impact of Covid-19 fiscal spending on climate change adaptation and resilience. *Nature Sustainability* 7(3): 270–281.

Silverman, A.I., T. Brain, B. Branco, P. sai venkat Challagonda, P. Choi, R. Fischman, K. Graziano, E. Hénaff, et al. 2022. Making waves: Uses of real-time, hyperlocal flood sensor data for emergency management, resiliency planning, and flood impact mitigation. *Water Research* 220: Article 118648.

Smucker, B., M. Krzywinski, and N. Altman. 2019. Two-level factorial experiments. *Nature Methods* 16(3): 211–212.

Suresh, N., T. Mishra, and D. Parthasarathy. 2024. The impact of floods and cyclones on fiscal arrangements in India: An empirical investigation at the sub-national level. *International Journal of Disaster Risk Reduction* 110: Article 104620.

Tang, D., J. Li, Z. Zhao, V. Boamah, and D.D. Lansana. 2023. The influence of industrial structure transformation on urban resilience based on 110 prefecture-level cities in the Yangtze River. *Sustainable Cities and Society* 96: Article 104621.

Tang, L.C., and L. Shen. 2024. Resilience indices from a family of recovery functions. *Fundamental Research* 4(1): 13–20.

Therias, A., and A. Rafiee. 2023. City digital twins for urban resilience. *International Journal of Digital Earth* 16(2): 4164–4190.

Tierney, K., and M. Bruneau. 2007. Conceptualizing and measuring resilience: A key to disaster loss reduction. *TR News* 250: 14–17.

UNDRR (United Nations Office for Disaster Risk Reduction). 2021. The human cost of disasters: An overview of the last 20 years (2000–2019). https://www.preventionweb.net/files/74124_humancostofdisasters20002019reportu.pdf. Accessed 16 Feb 2025.

Wang, M., Y. Fang, and C. Sweetapple. 2021. Assessing flood resilience of urban drainage system based on a "do-nothing" benchmark. *Journal of Environmental Management* 288: Article 112472.

Wang, J., J. Huang, H. Yang, and D. Levinson. 2022. Resilience and recovery of public transport use during Covid-19. *npj Urban Sustainability* 2(1): Article 18.

Wang, Q., S. Shen, H. Li, and X. Zang. 2024. Resilience evaluation research on coping with rainstorm inundation under the perspective of full cycle: A case study of Beijing-Tianjin-Hebei region. *Sustainable Cities and Society* 108: Article 105474.

Wu, Z., Y. Chen, X. Zheng, S. Huang, C. Duan, and P. Wang. 2024. A novel framework for evidence-based assessment of flood resilience integrating multi-source evidence: A case study of the Yangtze River Economic Belt, China. *Ecological Indicators* 167: Article 112705.

Wu, J., Y. Li, N. Li, and P. Shi. 2018. Development of an asset value map for disaster risk assessment in China by spatial disaggregation using ancillary remote sensing data. *Risk Analysis* 38(1): 17–30.

Xu, S., H. Chen, A.W.-K. Law, F. Zhu, D. Martini, and M. Lim. 2024. Development of a standardised framework with universal core indicators for flood resilience assessment. *Natural Hazards* 120(12): 10753–10772.

Xu, K., X. Zhang, L. Bin, and R. Shen. 2024. An improved global resilience assessment method for urban drainage systems: A case study of Haidian Island, South China. *Journal of Environmental Management* 360: Article 121135.

Yabe, T., P.S.C. Rao, S.V. Ukkusuri, and S.L. Cutter. 2022. Toward data-driven, dynamical complex systems approaches to disaster resilience. *Proceedings of the National Academy of Sciences* 119(8): Article e2111997119.

Yao, Q., J. Wang, M. Li, M.-P. Kwan, and J. Yin. 2025. Cross-regional and multi-entity resource coordination can enhance the supply of disaster relief materials during flood events in China. *Communications Earth & Environment* 6(1): Article 472.

Yin, D., Y. Chen, H. Jia, Q. Wang, Z. Chen, C. Xu, Q. Li, W. Wang, et al. 2021. Sponge city practice in China: A review of construction, assessment, operational and maintenance. *Journal of Cleaner Production* 280: Article 124963.

Zhang, H., J. Yang, L. Li, D. Shen, G. Wei, H. ur R. Khan, and S. Dong. 2021. Measuring the resilience to floods: A comparative analysis of key flood control cities in China. *International Journal of Disaster Risk Reduction* 59: Article 102248.

Zhang, Y., S. Song, X. Li, S. Gao, and M. Raubal. 2024. Leveraging context-adjusted nighttime light data for socioeconomic explanations of global urban resilience. *Sustainable Cities and Society* 114: Article 105739.

Zhang, J., H. Wang, J. Huang, Y. Wang, and G. Liu. 2023. A study on dynamic simulation and improvement strategies of flood resilience for urban road system. *Journal of Environmental Management* 344: Article 118770.

Zhang, P., S. Yang, J. Huang, and S. Hu. 2025. Block-scale modeling of residential land prices: Incorporating multilevel determinants and explainable artificial intelligence. *Habitat International* 156: Article 103283.

Zhou, Q., and Z. Qi. 2023. Urban economic resilience and human capital: An exploration of heterogeneity and mechanism in the context of spatial population mobility. *Sustainable Cities and Society* 99: Article 104983.

Zhu, S., D. Li, M. Chen, and Y. Zhang. 2024. Climate change scenario simulations for urban flood resilience with system dynamics approach: A case study of smart city Shanghai in Yangtze River Delta region. *International Journal of Disaster Risk Reduction* 112: Article 104801.

Zhuang, L., M. Wang, Z. Zhang, and K. Liu. 2024. Measurement of multidimensional reconstruction fund planning on the effectiveness of urban post-disaster recovery and reconstruction using indirect economic impact. *Environmental Impact Assessment Review* 105: Article 107365.

Zhuang, L., Z. Zhang, M. Wang, K. Liu, C. Liu, and W. Wu. 2024. Investigating the role of refining urban flood direct loss in enhancing the accuracy of indirect economic loss assessment. *International Journal of Disaster Risk Reduction* 102: Article 104285.